Unraveling Brainstem Deformations in Joubert Syndrome: A Statistical Shape Analysis of MRI-Derived Structures

Francesca Maccarone[1,2][0009−0004−6221−2671] ⋆, Giorgio Longari[1][0000−0002−2086−9091], Filippo Arrigoni[3][0000−0002−5508−1149], Denis Peruzzo[2][0000−0002−9480−379X], and Simone Melzi[1][0000−0003−2790−9591]

[1] University of Milano-Bicocca, Milan, Italy
[2] Neuroimaging Unit, Scientific Institute, IRCSS Eugenio Medea, Bosisio Parini, Italy
[3] Pediatric Radiology and Neuroradiology Department, Children's Hospital V. Buzzi, Milan, Italy

Abstract. Statistical shape analysis (SSA) is a powerful tool for studying anatomical structures and their geometric variations in medical imaging. In this work, we analyze real MRI-derived data to explore correlations between geometric deformations and Joubert syndrome (JS). Building on prior SSA research, we tailor the preprocessing pipeline to an in-house dataset and perform a detailed shape variability analysis using principal component analysis (PCA). A random forest classifier is then applied, achieving high classification accuracy. To ensure robustness, we test multiple train-test splits and evaluate their impact. In addition, we support clinical interpretation by providing visualizations that combine 3D and 2D information, resembling typical diagnostic paradigms on MRI planes. Our work offers some methodological insights into shape-based analysis and aims to serve as a practical tool for the medical community. Code and data are openly available at: https://github.com/Franca-exe/SSA-brainstem

Keywords: Statistical Shape Analysis· Brainstem Deformations· 3D Shape Matching.

1 Introduction

SSA plays a crucial role in medical imaging, enabling the study of anatomical structures and their geometric variations across different populations. This tool has multifaceted applications, ranging from pathology identification and characterization, creation of population templates, and image segmentation to surgical planning.

In this work, we focus on the brainstem, a key central nervous system structure that connects the brain to the spinal cord, serving as the main gateway for motor coordination and cognitive functions. We aim to analyze its geometric deformations and investigate potential correlations with JS, a rare congenital

---

⋆ Corresponding author: f.maccarone1@campus.unimib.it

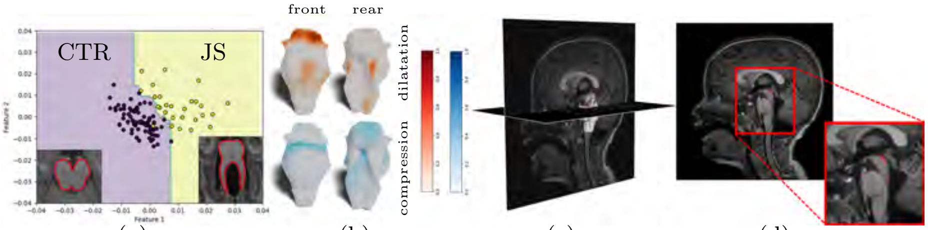

(a) (b) (c) (d)

Fig. 1. The multiple outputs of our pipeline: (a) binary classification discriminating JS patients from CTR; (b) local deformations on 3D shape, with dilation in red and compression in blue; (c) our 3D visualization of brainstem deformations (red) aligned with MRI planes; d) projected 3D brainstem deformation (red) on MRI slice.

condition defined by a characteristic cerebellar and brainstem malformation pattern known as "*Molar Tooth Sign*" (MTS) [20, 26].

Current clinical practice for the diagnosis of JS is primarily based on visual inspection of 2D axial MRI slices and identification of MTS (Fig.1(a)). However, image orientation and the presence of artifacts can lead to incorrect or inconclusive assessment, hindering the diagnostic process.

The dataset we examine consists of MRI-derived surface representations of the brainstem. These surfaces exhibit a relatively low mesh density and a high-frequency noise as we used a retrospective dataset that was not optimized for the brainstem analysis, and there are currently no software tools focusing on brainstem shape extraction. To characterize geometric variations, we focus on efficiency and data refinement through a remeshing procedure and denoising techniques to improve statistical analysis. We employ PCA to decompose shape deformations into meaningful modes. We systematically analyze these components to determine whether they encode anatomical features or pathological differences. We further assess their predictive power in distinguishing JS patients from healthy controls (CTR), exploring the stability of our findings across different dataset splits. Our contributions are threefold:

- A shape-based analysis of the brainstem from real MRI-derived data, with a fine-tuned preprocessing tailored to our data (Sec. 3).
- A systematic evaluation of PCA components to identify pathology-relevant variations and provide classification (Sec. 4).
- A tool for informative visualizations combining both 3D surface representations and 2D MRI planes (Sec. 5).

Through these analyses, whose outputs are summarized in Fig.1, we enhance the understanding of anatomical variations in JS supporting the neuroradiologists in the complex task of detecting and characterizing such a peculiar pathological condition. At the same time, we provide methodological insights into shape-based statistical modeling for medical imaging, taking a step further in the clinical translation of this powerful tool.

2 Related Work

2.1 Discrete Shape Processing

We define shapes as two-dimensional smooth manifolds embedded in $\mathbb{R}^3$, denoted using a calligraphic font (e.g., $\mathcal{S}$). In its discrete representation, a surface $\mathcal{S}$ can be approximated as a triangular mesh $\mathcal{S} = (V_{\mathcal{S}}, E_{\mathcal{S}})$, where $V_{\mathcal{S}}$ is the set of $n_{\mathcal{S}} \in \mathbb{N}$ vertices, $E_{\mathcal{S}}$ is the set of edges that connect vertices and form triangular faces. We define the matrix $X_{\mathcal{S}} \in \mathbb{R}^{n_{\mathcal{S}} \times 3}$, which contains the 3D coordinates of the vertices in $V_{\mathcal{S}}$, one row for each vertex.

The Laplace-Beltrami Operator (LBO) is the differential operator that extends the Laplacian to the manifold setting. We denote with $\Delta_{\mathcal{S}} \in \mathbb{R}^{n_{\mathcal{S}} \times n_{\mathcal{S}}}$ the matrix that discretizes the LBO of $\mathcal{S}$ [22,25]. The eigendecomposition of this matrix gives rise to a set of eigenvectors $\Phi_{\mathcal{S}} = \{\phi_1^{\mathcal{S}}, \phi_2^{\mathcal{S}}, \dots\}$ and the corresponding ordered eigenvalues $\{\lambda_1^{\mathcal{S}} \leq \lambda_2^{\mathcal{S}} \leq \dots\}$. The truncated set of the first $k \in \mathbb{N}$ eigenvectors of the LBO is commonly used as a basis to approximate the functions defined on $\mathcal{S}$, similarly to the low-pass approximation provided by Fourier analysis on Euclidean domains [14,15,31,32].

Given a pair of shapes, $\mathcal{S}_1$ and $\mathcal{S}_2$, with a common global semantic structure (e.g. the same organ from two different patients), shape-matching aims to find a pointwise correspondence $\Pi_{12} : \mathcal{S}_1 \rightarrow \mathcal{S}_2$, which assigns to each vertex $x \in \mathcal{S}_1$ a vertex $y \in \mathcal{S}_2$. Standard shape-matching solutions directly estimate the vertex-to-vertex map Π_{12}. The functional maps framework [24] (FMAPs), instead, focuses on the functional spaces defined on the surfaces, respectively $F(\mathcal{S}_1)$ and $F(\mathcal{S}_2)$. FMAPs exploits the fact that a given point-wise correspondence Π_{12} uniquely induces an operator $T_{21} : F(\mathcal{S}_2) \rightarrow F(\mathcal{S}_1)$, between the functional spaces, namely the *functional map*. Fixing a pair of bases for the spaces $F(\mathcal{S}_1)$ and $F(\mathcal{S}_2)$, the functional map T_{21} is represented by a small matrix C_{21} which is easier to optimize with respect to Π_{12}. Then, from C_{21}, FMAPs propose a procedure to recover an approximation of Π_{12}. The common choice for the bases is the truncated subset of k eigenvectors of the LBO. ZoomOut [21] is a refinement technique that improves the quality of the estimated Π_{12} by iteratively increasing the size of the bases. In [10], the authors proposed a version of ZoomOut to obtain correspondence among a collection of shapes. In SSA, we are interested in discovering the deformations that occur within a collection of shapes $\{\mathcal{S}_i\}_{i=1}^q$. To compute these deformations, it is usually necessary to fix a reference shape $\mathcal{M}$, estimate a correspondence between each shape and $\mathcal{M}$, and finally compute, for each vertex of $\mathcal{M}$, the 3D displacement to its corresponding vertex on each $\mathcal{S}_i$. Similarly to FMAPs, the shape difference operator [8,27] is a compact functional-based representation of the deformation between two shapes.

2.2 Statistical Shape Analysis

SSA quantifies anatomical variations, providing morphological descriptors for disease characterization, population modeling, and surgical planning. Traditional statistical approaches, such as geometric morphometrics, rely on the placement of landmarks and the evaluation of their variability using rigid and non-rigid registration methods. While providing a compact representation of the data, landmark-based approaches suffer from a strong dependence on landmarks positioning and topological discrepancies [29]. To overcome these limitations, alternative landmarks-free methods have been proposed [1, 5]. Critical for SSA is the role of shape matching, traditionally performed via methods such as Generalized Procrustes Analysis and Thin-Plate Spline Warping [3]. However, since the introduction of the functional maps framework [24] and its various extensions [10, 21], SSA has started to benefit from spectral methods, allowing accurate correspondences, computational efficiency and great flexibility.

Besides being a cross-disciplinary field with an enormous range of applications, SSA plays a key role in medical imaging, supported by a rich body of literature. Within the clinical framework, SSA can be used in the diagnosis, quantitative characterization and monitoring of pathological conditions, as well as in the definition of population priors for segmentation or image elaborations, in surgical planning and in prosthetic designs. Studies examine different anatomical regions, such as brain structures [28, 30], skull and cranial bones [13, 19], cardiovascular system [2].

2.3 Joubert Syndrome and Central Nervous System

Joubert syndrome is a rare neurodevelopmental group of disorders with an incidence of 1 in 100,000 [7, 23]. JS exhibits a significant heterogeneity from clinical, neurogenetic and neuroimaging points of view. However, the MTS and vermian hypoplasia (VH), resulting in distortion and enlargement of the fourth ventricle, as depicted in Fig.1(a), are consistent findings in neuroimaging acquisitions [23, 26]. In particular, MTS is the hallmark of the syndrome, and its identification is essential for a diagnosis, though its shape and extension may vary. As described in [20], MTS is the consequence of a pattern of cerebellar and brainstem malformations, including midbrain widening, deepening of the interpeduncular cistern and a thickening and horizontal orientation of the superior cerebellar peduncles.

MRI acquisitions with T1 and T2-weighted images (respectively, T1W and T2W) [16] are the main diagnostic images, as JS identification is still mainly based on visual inspection of a series of 2D images [12, 23, 26], which does not fully account for the inherently 3D nature of the examined structures, in addition to the limitations introduced in (Sec. 1). Although JS alters the geometry of anatomical structures, especially infratentorial ones, to the best of our knowledge, no studies have applied statistical shape analysis in this context.

3 Analysis of the Collection of Shapes

Our study deals with a collection of brainstem shapes to perform SSA on it. As described in the following, we leverage previous works, modifying fundamental steps to target a clinically relevant context. In particular, we propose a novel preprocessing step and fine-tune shape-matching initialization to efficiently achieve accurate correspondences.

3.1 Data Acquisition and Preparation

We consider an initial dataset of n_{SUB}= 124 subjects, including n_J = 32 JS patients (mean age: 10.1 ± 8.6 years) and n_{CTR}= 88 healthy subjects (mean age: 13.8 ± 3.2 years), who undergo an MRI scan session. All images are acquired on a 3T Achieva dStream MR scanner (Philips Medical Systems), and the acquisition protocol includes a 3D T1W sequence (voxel size $1 \times 1 \times 1$ mm^3, TR=8.3ms, TE=3.9ms; flip angle=8°). The study has been approved by the Ethics Committee of E. Medea Research Institute. The legal representatives of all the participants have provided written informed consent.

We extract binary brainstem masks from T1W images using FreeSurfer [4] and visually inspect them to correct major segmentation errors and discard poorly segmented subjects (4 in total). We crop the lower edge of the masks, maintaining a fixed brainstem height of around 80 mm to account for the different positions of the field of view among subjects. Using 3D Slicer [6], we convert segmentations to triangular meshes of around 6000 vertices. We remove disconnected components, ensure manifoldness, and remesh shapes at around 3000 vertices by leveraging the preprocessing step from [18].

3.2 Rigid Registration

After area normalization and barycenter alignment, which are canonical preprocessing steps, we perform rigid registration of the shapes in our collection. Given that the brainstem shapes primarily elongate along one direction, we estimate the subject-specific primary axis as the first principal component of PCA computed on the coordinates of the vertices. We align each pair of shapes by applying the minimum rotation between their first principal directions. As explained in (Sec. 4), this rotation angle represents an important feature that highly correlates with the occurrence of the pathology. This registration step is designed explicitly for the brainstem shapes. It allows us to substitute the computationally inefficient estimation of the FMAPs initialization [17] (FPS in Table 1) with a more efficient K-nearest neighbor (KNN) search in the 3D space, with $K = 1$.

3.3 Network Model

Our pipeline is inspired by previous methods [17, 19], where SSA is performed on medical datasets exploiting FMAPs. These studies demonstrate that deformations extracted from a collection of shapes carry highly informative signals, and, building on these results, we aim to utilize this strategy to recognize patients affected by JS. As in [17], the first step of the pipeline employs *ReMatching* [18], not only to rescale from high-density shapes but rather to reduce the high-frequency noise introduced by the volume discretization in the MRI images, granting a correspondence between shapes also at the original resolution. Next, the rest of the pipeline builds upon the creation of a graph, where each node corresponds to a shape $\mathcal{S}_i$ and each edge encodes a correspondence T_{ij} encoded by FMAPs between $\mathcal{S}_i$ and $\mathcal{S}_j$. We test different numbers of edges in the graph

Table 1. Comparison of KNN (Ours) and FPS ([17]) initialization methods for shape collection matching at different numbers of network edges. Evaluation is reported in terms of Chamfer Distance and computational runtime (time) expressed in seconds.

	250 edges		500 edges		1000 edges		2000 edges	
Method	Chamfer	time	Chamfer	time	Chamfer	time	Chamfer	time
KNN (**Ours**)	0.02779	1054	0.02595	2048	0.02595	4308	0.02594	10990
FPS [17]	0.02714	2460	0.02609	5826	0.02727	10863	0.02728	19234

network (250, 500, 1000, 2000), always ensuring that the graph is connected. For every edge T_{ij} in the graph, the method also considers the edge in the opposite direction T_{ji} to enforce bijectivity. We evaluate these correspondences in (Sec. 5). The estimation of the correspondence is composed of the following steps. We first rigidly align the shapes, as described in (Subsec. 3.2), and compute an initial pointwise correspondence for all the shapes connected by an edge by applying the nearest neighbor search among vertices in $\mathbb{R}^3$. Then, we encode these correspondences exploiting FMAPs and apply the ZoomOut algorithm for shape collections [10] to refine them, improving the overall mapping precision. The accuracy of the calculated functional maps directly impacts the reliability of shape matching. Unlike [17], we follow the original Zoomout approach [21], upsampling the map by only one eigenfunction at each step, reaching a final dimension of 60. This choice is motivated by the expectation of significant non-isometric variations within the shape collection due to pathological deformations. By fostering [9] in the iterative refinement process, we obtain the *limit shape* that is an abstract functional representation of the average shape of the collection. As done in [17, 19], we select from the collection the shape which has the most similar functional representation to the limit shape as the mean shape $\mathcal{M}$. Fixing $\mathcal{M}$ and exploiting the correspondence between $\mathcal{M}$ and each shape in the collection provided by [9], we can compute a deformation field that deforms $\mathcal{M}$ into each shape $\mathcal{S}_i$. Finally, we apply PCA to these deformation fields, obtaining a compact representation of the variations that occur in the collection. In Table 1, we report the evaluation of the estimated correspondence between $\mathcal{M}$ and each $\mathcal{S}_i$. In the absence of ground truth correspondences, we adopt the Chamfer distance [17] to evaluate the estimated correspondences, averaged over all $\mathcal{S}_i$.

4 Classification

In this section, we present some potential applications of SSA. Specifically, we apply a PCA decomposition both to reduce the dimensionality of each subject representation in the mapping model and to identify deformation patterns encoding relevant pathology-related information. PCA coefficients are subsequently used for classification and visualization tasks.

All the PCA coefficients deriving from displacements and the rotation corrections performed in the rigid alignment (Sec. 3.2) are fed to a Random Forest (RF) classifier. As our dataset has an unbalanced patient/control ratio, we set

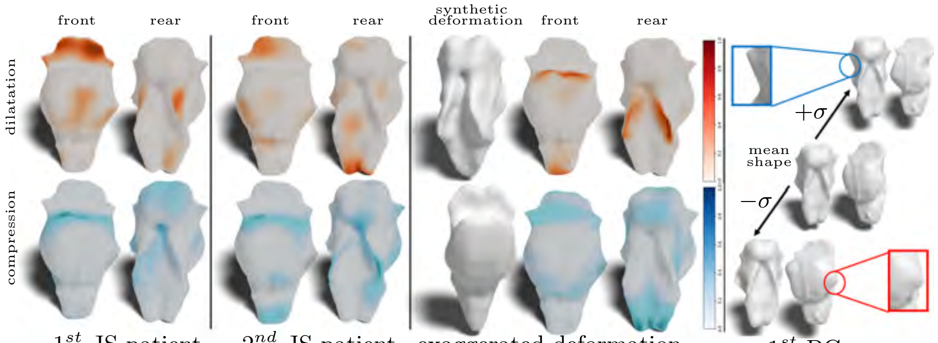

1^{st} JS patient 2^{nd} JS patient exaggerated deformation of a template 1^{st} PC

Fig. 2. Visualization of median shape deformations as it morphs into different JS patients and a synthetically deformed FreeSurfer brainstem template [4] used to test the method's sensitivity to local changes. The rightmost panel shows variations along the first PC with an explicative close up on local deformations.

the RF weight coefficient $w_J = 3$ to ensure greater importance to patient samples during training. For completeness, we also investigated the results setting it to $w_J = 2.5$ and 3.5. We evaluate the classifier performances applying an 8-fold cross-validation procedure with a training/testing sample size split of 105 to 15 subjects, ensuring that each subject is included in the test set once. To highlight the simplicity of the classifier while demonstrating the quality of the features extracted by the network, we just set the number of trees in the forest to 100 without tuning any other parameter. All the experiments are performed using Python 3.11.9-version code tested on a machine with an AMD RYZEN 5000 series 7 CPU, 16 GB RAM.

5 Results and Discussion

Table 1 reports the results in terms of the Chamfer distance of the experiments for estimating the correspondence between the mean shape and each shape in the collection (Sec. 3). Increasing the number of edges in the network improves mapping accuracy, but with more than 500 edges the metric stabilizes showing minimal improvements, while the computational time linearly increases with the number of edges. Moreover, the FPS initialization based on FMAPs does not yield better results in terms of Chamfer distance, while it increases computational cost. These results suggest that, in this context, a network with 500 edges and our initialization method are the most cost-effective solutions. However, to further maximize computational cost efficiency with minimal loss in quality, we set the number of edges to 250 for the classification experiment.

Classification performances are summarized in Table 2, showing that a simple RF classifier correctly identifies JS patients based on the SSA-derived features, without the need for specific parameter tuning. The 8-fold cross-validation procedure, assessing generality, consistently achieves strong classification scores. Analyzing the weights assigned to each feature, we observe that, in each cross-

Table 2. Average classification metrics from 8-fold cross-validation for correctly classifying JS. In the table headers, we shortened Accuracy as Acc.

Weight	Acc.	Balanced Acc.	Precision	Sensitivity	Specificity	F1
2.5	92.50	89.91	87.75	84.37	95.455	84.626
3	91.75	90.34	84.63	87.50	93.182	84.375
3.5	91.63	88.71	82.13	90.63	92.046	85.375

validation fold, the RF model estimates that the rigid rotation (Subsec. 3.2) contributes approximately 10% to correctly classify the subjects and is the second most important feature. Moreover, we observe that the other highest contributions are assigned to the first ten PCs, indicating that they capture the most relevant deformations characterizing JS. This aligns with the PCA compactness analysis, which shows that the first ten principal components, namely the principal deformations, explain around 80% of the total shape variability, primarily encoding localized deformations. Specifically, the first component represents dilation/contraction at the level of the pons (rightmost panel in Fig.2). These results demonstrate that the implemented SSA pipeline correctly encodes the deformation patterns associated with JS and that the proposed optimization solutions improve the accuracy in assessing shape correspondences while reducing the computational time, making the tool more efficient and flexible.

For completeness, we investigate statistical shape modeling (SSM) as a viable alternative for representing shape variability within our dataset. Traditional SSM methodologies are excluded due to inherent drawbacks, including strong prior assumptions on shape variability and significant computational demands. Instead, we test one of the latest learning-based approach in the field, namely Mesh2SSM [11]. However, empirical evaluation shows that Mesh2SSM is approximately 24 times slower than our method and exhibits poor performance on limited sample sizes, making it unsuitable for our aim of developing a lightweight and scalable pipeline in a scenario with a small dataset.

We further expand the potential of our approach with different smart visualization examples (both 3D and 2D), providing visualization of subject-specific deformation analysis results on the 3D shape (Fig.2), or integrating (Fig.1(c)) and projecting (Fig.1(d)) this information onto the original anatomical images, supporting clinicians in the diagnostic process. The visual inspection of the subject-specific analysis (Fig.2) confirms that all of the major deformations reported for each subject are located coherently with the main alterations associated with JS, with the exception of the inferior bound. In particular, we reported reductions of the brainstem pons, alterations of the cerebellar peduncle interface and dilatations of the mesencephalon.

The main limitations of our work are related to the use of MRI data and shape extraction pipelines not optimized for the analysis of the brainstem, resulting in noisy shapes, that can be further improved in future studies.

6 Conclusion

This study applies an optimized, learning-free, and efficient SSA pipeline in the context of a rare disease, where the available data is inherently limited. We demonstrate the efficacy of SSA in modeling variations of a key structure of the central nervous system (i.e. the brainstem) and in identifying deformation patterns associated with JS. We show that PCA can be used to extract informative features to identify pathological cases, taking a step further towards the clinical translation of advanced analysis tools such as SSA. The proposed pipeline can be further optimized to the medical image context, for example improving the selection of the mean shape or testing different classifiers. Finally, we plan to scale our pipeline to other brain structures and clinical conditions to build a tool for the detection and quantitative characterization of brain malformations, supporting both clinical practice and research.

Acknowledgments. This work was partially funded by the European Union – Next Generation EU within the project NRPP M4C2, Investment 1.,3 DD. 341 - 15 March 2022 – FAIR – Future Artificial Intelligence Research – Spoke 4 - PE00000013 - D53C22002380006 and supported by UniverLecco and by Italian Ministry of Health (Ricerca Corrente “2025” to Denis Peruzzo)

Disclosure of Interests. The authors have no competing interests to declare that are relevant to the content of this article.

References

1. Biasotti, S., Cerri, A., Bronstein, A., Bronstein, M.M.: Recent trends, applications, and perspectives in 3d shape similarity assessment. Computer Graphics Forum **35**, 87–119 (2015)
2. Biglino, G., Capelli, C., Bruse, J., Bosi, G.M., Taylor, A.M., Schievano, S.: Computational modelling for congenital heart disease: how far are we from clinical translation? Heart **103**(2), 98–103 (2017)
3. Brombin, C., Salmaso, L.: A Brief Overview on Statistical Shape Analysis, pp. 1–16. Springer New York, New York, NY (2013)
4. Dale, A., Fischl, B., Sereno, M.: Cortical surface-based analysis. i. segmentation and surface reconstruction. NeuroImage **9**(2), 179—194 (February 1999)
5. Dupej, J., Bárá, V., Velemínská, D., Pelikán, J.: Statistical mesh shape analysis with nonlandmark nonrigid registration. In: Proceedings of the 12th International Conference on Computer Graphics and Artificial Intelligence (3IA). pp. 1–8 (2014)
6. Fedorov, A., Beichel, R., Kalpathy-Cramer, J., Finet, J., Fillion-Robin, J.C., Pujol, S., Bauer, C., Jennings, D., Fennessy, F., Sonka, M., Buatti, J., Aylward, S., Miller, J.V., Pieper, S., Kikinis, R.: 3d slicer as an image computing platform for the quantitative imaging network. Magnetic Resonance Imaging **30**(9), 1323–1341 (2012), quantitative Imaging in Cancer
7. Forsyth, R., Parisi, M.A., Altintas, B., Malicdan, M.C., Vilboux, T., Knoll, J., Brooks, B.P., Zein, W.M., Gahl, W.A., Toro, C., Gunay-Aygun, M.: Systematic analysis of physical examination characteristics of 94 individuals with joubert syndrome: Keys to suspecting the diagnosis. American Journal of Medical Genetics Part C: Seminars in Medical Genetics **190**(1), 121–130 (2022)

8. Huang, R., Chazal, F., Ovsjanikov, M.: On the stability of functional maps and shape difference operators. Computer Graphics Forum **37**(1), 145–158 (2018)
9. Huang, R., Achlioptas, P., Guibas, L., Ovsjanikov, M.: Limit shapes – a tool for understanding shape differences and variability in 3d model collections. Computer Graphics Forum **38**(5), 187–202 (2019)
10. Huang, R., Ren, J., Wonka, P., Ovsjanikov, M.: Consistent zoomout: Efficient spectral map synchronization. Computer Graphics Forum **39**(5), 265–278 (2020)
11. Iyer, K., Elhabian, S.Y.: Mesh2ssm: From surface meshes to statistical shape models of anatomy. In: Medical Image Computing and Computer Assisted Intervention – MICCAI 2023. pp. 615–625 (2023)
12. Kendall, B., Kingsley, D., Lambert, S.R., Taylor, D., Finn, P.: Joubert syndrome: a clinico-radiological study. Neuroradiology **31**(6), 502–506 (1990)
13. Larsen, R., Hilger, K.B., Wrobel, M.C.: Statistical 2d and 3d shape analysis using non-euclidean metrics. In: Medical Image Computing and Computer-Assisted Intervention - MICCAI 2002. Lecture Notes in Computer Science, vol. 2489, pp. 428–435. Springer (2002)
14. Levy, B.: Laplace-beltrami eigenfunctions towards an algorithm that "understands" geometry. In: IEEE International Conference on Shape Modeling and Applications 2006 (SMI'06). pp. 13–13 (2006)
15. Lévy, B., Zhang, H.: Spectral mesh processing. In: ACM SIGGRAPH 2010 Courses, pp. 1–312. Association for Computing Machinery (2010)
16. Liao, D.w., Zheng, X.: Analysis of ct and mri manifestations of joubert syndrome. Journal of the Belgian Society of Radiology (Sep 2023)
17. Maccarone, F., Longari, G., Viganò, G., Peruzzo, D., Maggioli, F., Melzi, S.: S4a: Scalable spectral statistical shape analysis. In: Smart Tools and Applications in Graphics - Eurographics Italian Chapter Conference. The Eurographics Association (2024)
18. Maggioli, F., Baieri, D., Rodolà, E., Melzi, S.: Rematching: Low-resolution representations for scalable shape correspondence. In: Computer Vision – ECCV 2024. pp. 183–200. Springer Nature Switzerland, Cham (2025)
19. Magnet, R., Bloch, K., Taverne, M., Melzi, S., Geoffroy, M., Khonsari, R.H., Ovsjanikov, M.: Assessing craniofacial growth and form without landmarks: A new automatic approach based on spectral methods. Journal of Morphology **284**(8) (2023)
20. Maria, B.L., Hoang, K.B., Tusa, R.J., Mancuso, A.A., Hamed, L.M., Quisling, R.G., Hove, M.T., Fennell, E.B., Booth-Jones, M., Ringdahl, D.M., Yachnis, A.T., Creel, G., Frerking, B.: "joubert syndrome" revisited: Key ocular motor signs with magnetic resonance imaging correlation. Journal of Child Neurology **12**(7), 423–430 (1997), pMID: 9373798
21. Melzi, S., Ren, J., Rodolà, E., Sharma, A., Wonka, P., Ovsjanikov, M.: Zoomout: spectral upsampling for efficient shape correspondence. ACM Transactions on Graphics (TOG) **38**(6), 1–14 (2019)
22. Meyer, M., Desbrun, M., Schröder, P., Barr, A.H.: Discrete Differential-Geometry Operators for Triangulated 2-Manifolds. In: Visualization and mathematics III, pp. 35–57. Springer, New York, NY (2003)
23. Montero Torres, J.A., Flores Escobar, B., Guzman Martinez, J., Barrera Martínez, R.A., Hernández Cortez, F.P.: Radiological features of joubert syndrome and clinical case presentation. Radiology Case Reports **19**(10), 4167–4172 (2024)
24. Ovsjanikov, M., Ben-Chen, M., Solomon, J., Butscher, A., Guibas, L.: Functional maps: a flexible representation of maps between shapes. ACM Transactions on Graphics (ToG) **31**(4), 1–11 (2012)

25. Pinkall, U., Polthier, K.: Computing Discrete Minimal Surfaces and their Conjugates. Experimental mathematics **2**(1), 15–36 (1993)
26. Poretti, A., Huisman, T., Scheer, I., Boltshauser, E.: Joubert syndrome and related disorders: Spectrum of neuroimaging findings in 75 patients. American Journal of Neuroradiology **32**(8), 1459–1463 (2011)
27. Rustamov, R.M., Ovsjanikov, M., Azencot, O., Ben-Chen, M., Chazal, F., Guibas, L.: Map-based exploration of intrinsic shape differences and variability. ACM Transactions on Graphics (TOG) **32**(4), 1–12 (2013)
28. Shen, L., Cong, S., Inlow, M.: Chapter 13 - statistical shape analysis for brain structures. In: Zheng, G., Li, S., Székely, G. (eds.) Statistical Shape and Deformation Analysis, pp. 351–378. Academic Press (2017)
29. Srivastava, A., Joshi, S.H., Mio, W., Liu, X.: Statistical shape analysis: Clustering, learning, and testing. IEEE Transactions on Pattern Analysis and Machine Intelligence **27**(4), 590–602 (2005)
30. Styner, M., Oguz, I., Xu, S., Brechbühler, C., Pantazis, D., Levitt, J., Shenton, M., Gerig, G.: Statistical shape analysis of brain structures using spharm-pdm. The insight journal **1071**, 242–250 (07 2006)
31. Taubin, G.: Geometric Signal Processing on Polygonal Meshes. In: Eurographics 2000 - STARs. Eurographics Association (2000)
32. Taubin, G.: A Signal Processing Approach To Fair Surface Design, p. 351–358. SIGGRAPH '95, Association for Computing Machinery, New York, NY, USA, 1 edn. (1995)